Quantitative shape analysis of *in vivo* Kar9: droplet-like behaviour during fusion

McGill University

Name: Angela Zhao

Student Number: 260825942

Course: COMP 402

Supervisor: Dr. Jackie Vogel

Submitted: August 2022

1 Introduction

Liquid-liquid phase separation is the phenomenon by which proteins within a solution condense and form droplets. This is a critical process in many biological processes, including cellular organization. In this paper, we will look at fusion-like events of the Kar9 complexe in budding yeast that occur during spindle positioning in cell division. We will use the Elyra 7.2 SIM^2 system – a state-of-the-art microscopy system and one of the first of its kind in Canada – to capture fast, high-resolution images of *in vitro* fluorescent-tagged Kar9 protein for the first time. In this work, we will explore new software and shape-analysis techniques that are made possible by the fast time scale and high resolution of the Elyra 7.2 SIM^2 system. Comparable analyses are on the µm/min scale, whereas our study is on the nm/s scale. One caveat of the SIM^2 processing is that it is artifact-prone. Therefore, we will also describe a robust pipeline that uses machine-learning algorithms to accurately segment and analyze SIM^2 outputs. This technique can be easily adapted for other analyses of Elyra 7.2 SIM^2 data. By extracting information of the shape and comparing it to the known physical properties of droplets, we hope to determine whether or not the Kar9 protein displays liquid-like condensate behaviour during mitotic spindle positioning.

2 Background

2.1 Kar9 function and droplet properties

The budding yeast *Saccharomyces cerevisiae* is a useful model for studying mitotic microtubule (MT) specialization because it comprises functionally equivalent structures and proteins to vertebrates. Its mitotic spindle has an old spindle pole body (SPB) and a newly synthesized one. The old SPB synthesizes long astral microtubules that probe the bud cortex during spindle positioning (Chen et. al., 2019; Hotz et. al., 2012; Pereira, 2001) (Fig. 1A). This interaction relies on the MT +end tracking protein (+TIP) Kar9. Kar9 is a 74 kD protein (Miller & Rose, 1998) that is unusual among +TIPs because it follows the shrinking MT tip in addition to the growing one. One possible explanation for this behaviour, which has been confirmed *in vitro* (Meier et. al., 2021), is that it has the ability to form a liquid-like condensate. In addition, this belief is supported by Kar9's ability to self-associate. Kar9 possesses highly conserved interfaces where it binds to itself and other proteins. There are three binding interfaces (α, β, γ) at which it can interact with itself (Kumar et. al., 2021; Meier et. al., 2021) and a C-terminal domain that has one binding site for the Bik1 dimer (Moore et. al., 2006; Meier et. al., 2021) and at least three binding sites for the Bim1 dimer (Kumar et. al. 2021; Manatschal et. al., 2016; Zimniak et. al., 2009) (Fig. 1C). While there is molecular basis and *in vitro* evidence for droplet formation by Kar9, it is unknown if this remains true *in vivo*.

The behaviour of phase-separated droplets in viscous media has been well characterized theoretically and experimentally in non-biological experiments. In particular, we are concerned about the way droplets tend to deform during fusion-like events in living cells. When two droplets fuse, the aspect ratio – which is 1 for perfect circles, or >1 for non-circular ellipses – of the fused droplet is expected to decrease exponentially when it is plotted against time. This characteristic fusion dynamic has been previously confirmed in

other biological structures *in vivo* (Brangwynne et. al., 2011). Once two droplets touch, they form an energetically unfavourable dumbbell shape. The surface tension drives the fused droplet to return to a spherical shape (Fig. 1D). The time this process takes in a Newtonian fluid is called the characteristic time, τ, given by $\tau \approx (\eta/\gamma) \cdot l$, where η is the drop viscosity, γ is the surface tension, and l is the characteristic length of the drops (Eggers et. al., 1999). However, unlike in previous studies performed on the μm/min scale, Kar9 acts on the nm/s size and time scales. If, indeed, the fusion follows an exponential decay, the characteristic time against length plot should produce a linear trend, where the line approximates the ratio of viscosity and the surface tension of the droplet.
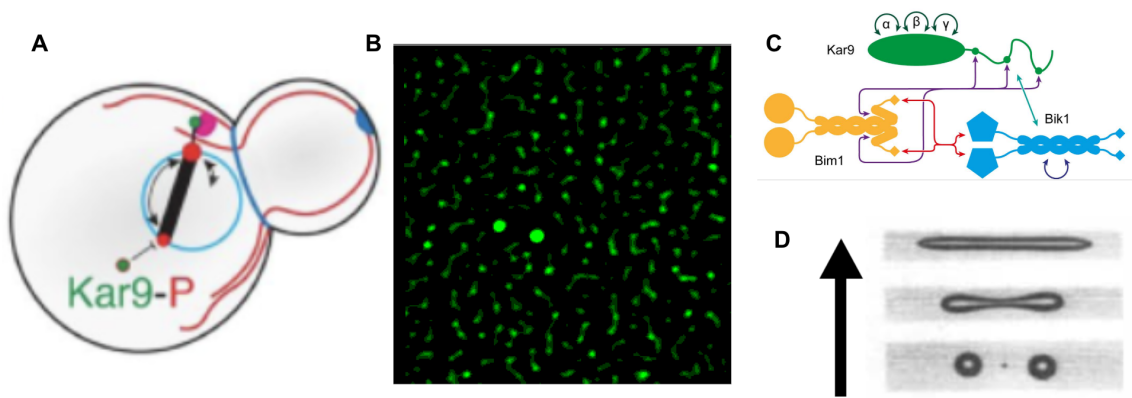

Figure 1. (A) Kar9 in budding yeast cell during mitotic spindle positioning (adapted from Meziane et. al., 2020). (B) Kar9-mNG captured by the Elyra 7.2 microscope and processed with SIM^2 using the parameters described in Section 3.1. (C) Diagram of the binding sites of the Kar9 complex (retrieved from Meier et. al. 2021). (D) Diagram of droplet fusion (adapted from Stone 1994.).

2.2 The Elyra 7.2 SIM² system

The Elyra 7.2 is a state-of-the-art microscopy system and one of the first of its kind in Canada. Building on the principles of structured illumination microscopy (SIM), the Elyra 7.2 is equipped with Lattice SIM^2, which allows us to resolve structures down to 60 nm (Zeiss, n.d.) – far beyond the diffraction limit of conventional microscopy. It still preserves the benefits of light microscopy by capturing cell dynamics at much higher speeds, up to 255 fps, than other super-resolution microscopy techniques, such as STED. We will use this system to capture the shape of fluorescently-labeled Kar9 through the course of its dynamic movements during spindle positioning.

However, the Elyra 7 system is not without fault. As with other super-resolution microscopy techniques, SIM^2 is prone to reconstruction artifacts (Schaefer et. al., 2004) (Fig. 1B). While these artifacts can be suppressed by adjusting the imaging parameters, such as reducing the exposure time of the laser, this will greatly reduce the signal-to-noise ratio of the captured images. Therefore, it makes more sense to deal with the artifacts during the post-acquisition data analysis steps.

2.3 TrackMate in ImageJ2

ImageJ2, or Fiji, is a Java-based image processing software. The TrackMate plugin is an automated tracking software that specializes in bioimage analysis, specifically bright field and fluorescent microscopy (Tinevez et. al., 2017). The plugin uses a detector to identify the pixels belonging to the region of interest, or spots, throughout a stack and then integrates deep learning algorithms to connect the spots in each slice to form tracks. During each step, the user can specify spot and track filters to more precisely isolate the regions of interest. In addition, TrackMate identifies useful features of each track and exports them to a CSV file. Some important features are signal-to-noise ratio (SNR) defined as

$$SNR = (I_{in} - I_{out}) \div std_{in} \quad \text{(Eq. 1)}$$

where I_{in} is the mean intensity inside the spot volume, I_{out} is the mean intensity from the volume between the ring of the spot circumference and a ring with double the radius of the spot. Std_{in} is the standard deviation of the intensities within the spot (Jaqaman et. al., 2008). Other interesting features include the intensity of the spot and the X, Y, Z locations. Different detectors may compute additional features. The current pipeline that the Vogel lab uses for analyzing similar fluorescent images utilizes the Difference of Gaussians detector and the Linear Assignment Problem tracker.

The Difference of Gaussians detector is a fast and robust detector that smoothes edges and removes shadows. The Linear Assignment Problem (LAP) tracker is ideal for Brownian motion particles or non-Brownian motion particles that are few in number and low in concentration (Jaqaman et. al., 2008). It serves to link the spots found in each slice of a stack. I will be using the LAP tracker for all analyses. Kar9 is attached to a microtubule and can exhibit both Brownian and non-Brownian motions. However, the fusion events studied will have at most two Kar9 complexes and Kar9 is sufficiently dilute in the cell for the LAP tracker.

The current pipeline makes some critical assumptions: (1) the spot is spherical, (2) the spot is always the same size, and (3) the size of the spot is known. These assumptions are not valid for fusion events, nor are they useful for the shape analysis we wish to perform. These assumptions are a consequence of the required inputs of the DoG detector.

3 Methods

3.1 Data collection

Wild type budding yeast were fluorescently tagged at Spc42 with mCherry and at Kar9 with mNeonGreen. 2-dimensional (2D), 200-second time series of the cells were collected using the ZEISS Elyra 7.2 microscope with the Plan-Apochromat 63x/1.4 Oil DIC M27 objective . The microscope settings were as follows: 561 nm laser at 2.0%, 488 nm laser at 5.0%, 25.0 ms camera exposure time. The resulting 16-bit images had a resolution of 1280

x 1280 pixels. The frame depth in Z is 200 nm. The data for this project was collected by Master student Katherine Morelli.

Next, I used the software Zen (black edition) to process the time series. I manually looked through maximum projections of the phases of the movies to identify potential fusion events. Fusion events look like two distinct Kar9-mNG spots that approach each other and conjoin to form one single spot. Then, I cropped the images in X, Y, and time to isolate Kar9 fusion events and to reduce the SIM^2 processing time, which was a significant bottleneck in our pipeline. The SIM^2 settings were as follows: 12 iterations, 0.1500 regularization weight, x2 proc. sampling, x2 out. sampling, and scale-to-raw to preserve the real pixel intensities. Only the green channel was processed to further reduce processing time.

3.2   ImageJ2 TrackMate Detectors

All movies were processed using the ImageJ2 TrackMate plug-in in order to detect the Kar9-mNeonGreen droplets.

3.2a   Difference of Gaussians detector

The DoG detector is TrackMate's default detector. The DoG detector calculates two sigmas for two gaussian filters

$$\sigma_1 \ = \ 1 \, / \, (1 \ + \ \sqrt{2}\,) \times d \quad \text{(Eq. 2)}$$

$$\sigma_2 \ = \ \sqrt{2} \times \sigma_1 \quad \text{(Eq. 3)}$$

where d is the expected diameter of the spot. The original image is then Gaussian filtered using the smaller sigma to remove small features, and another copy of the original image is filtered using the larger sigma to remove slightly larger features, so only the largest features
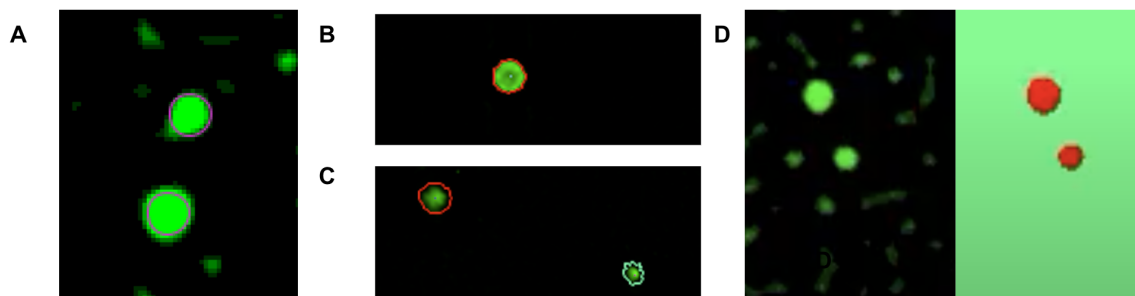

Figure 2. (A) Spots detected by the DoG TrackMate detector using a diameter of 290 nm. (B) TetraSpeck detected by the StarDist detector. Sometimes the contours are very reliable. (C) TetraSpeck detected by the StarDist detector. Sometimes the contours are very poorly approximated. (D) Original image of Kar9-mNG microscopy image (left) compared to segmentation results from Trainable Weka Segmentation using the model described in section 4.1 and with probability threshold of 0.8.

remain. Finally the larger Gaussian filtered image is subtracted from the smaller Gaussian

filtered one to produce a smooth image. It is important to note that when two spots are closer than d/2, the smaller of the two spots are discarded. Finally, the subpixel location is calculated using simple parabolic interpolation (Lowe, D., G., 2004).

The DoG detector is best used for spherical objects of fixed radius. It has fast time complexity and requires only one input: approximate spot size. However, the DoG detector makes assumptions that are not true for our fusing Kar9 droplets, namely it assumes fixed radius and spherical shape (Fig. 2A). As a result, we are not able to extract any useful information about the shape from this detector. Furthermore, the DoG tracker has low selectivity in the absence of additional spot filters. Therefore, the user must manually adjust the filters until all and only the spots of interest are detected.

3.2b   StarDist detector

The StarDist and Trainable Weka Segmentation (see section 3.2c) detectors overcome the significant caveats of the DoG detector. Firstly, they do not assume that the objects have spherical shapes and will work on both spherical and non-spherical objects. Secondly, they do not assume the objects have fixed radii. Finally, these detectors offer contour-specific features, such as ellipse aspect ratio, which I will use extensively for my analysis.

The StarDist detector is a modified version of the bounding box approach to segmentation (Liu et. al., 2016; Schmidt et. al., 2018). The objects of interest are first approximated by axis-aligned bounding boxes, then the shapes of the objects are refined by classifying each of the pixels within the boxes, usually through a convolutional neural network (He et. al., 2017). However, the box shape does not accurately describe circular shapes, such as cell nuclei and our Kar9 complexes. In the StarDist detector, Schmidt et. al. propose to use flexible star-convex polygons to approximate the shape in lieu of boxes. Their method has been shown to perform extraordinarily well on images with very crowded nuclei that do not have merging bordering cell instances (Schmidt et. al., 2018).

In my tests, the StarDist detector's performance was hit-and-miss. At times, it classified the border of the object very reliably (Fig. 2B), while other times the pentagon was clearly a poor approximation of the shape of the spot (Fig 2C). This can partly be attributed to the fact that our Kar9 complexes (and also the TetraSpeck beads shown in the figures) were 200-300 nm in diameter (manually measured using the ruler tool in ImageJ2). Since every pixel represents 31 nm, our droplets are approximately 10 pixels across. The StarDist detector has been shown to perform very poorly on objects with fewer than 10 pixels and much better on objects with hundreds of pixels (ImageJ, n.d.). Even with the super-resolution SIM[2] technique, the Kar9 complexes err on the lower end of that spectrum. Another point of observation is that the StarDist detector was not designed for merging objects (Schmidt et. al., 2018), but our fusion events are precisely that.

3.2c   Trainable Weka Segmentation detector

The Trainable Weka Segmentation (TWS) detector is, as the name suggests, a trainable machine learning tool for image segmentation. The Weka segmenter was originally designed to analyze electron microscope images and it is special in the fact that it requires very little ground truth (manual annotation) in order to train a reliable classifier for electron microscopy images (Arganda-Carreras et. al., 2017). This tool uses ImageJ2-native methods

to quantify the image features from the ground truth, represents these features as vectors, and trains a WEKA learning scheme on the features using fast forest quantile regression. The result is then applied to classify the remaining image data (Arganda-Carreras et. al., 2017). Image features are determined using edge detectors, texture filters, noise reduction filters, and membrane detectors, which can be chosen by the user. Because our Kar9 images have no discernible texture and SIM^2 processing already adds a level of noise reduction, I will only be using edge detectors to train the TWS model.

The TW segmenter also offers unsupervised learning/clustering schemes, but I will not use them for our data because supervised learning generally produces better and faster segmentation results. In addition, our background and feature classes are both quite stereotyped.

Once we have our trained model, we can import it into TrackMate and segment an image with one input: the probability threshold to accept a pixel as our target class. Through testing, I found that a probability threshold of 0.8 is ideal. Higher probability thresholds are too selective and create pixel lines such that the resulting aspect ratio (defined in section 3.3) exceeds 10 000, which does not reflect what we already know to be true about the shape of the Kar9 protein complexe, nor does it reflect what is visually observed from the microscopy images. On the other hand, lower probability thresholds are not selective enough and could potentially include some background on select samples.

The TWS detector performs best on our samples. It stays very loyal to the true borders of our Kar9 complexes (Fig. 2D). For this reason, all the analysis will be performed using the TWS detector.

3.3   Analyzing and visualizing tracking results

The output of TrackMate is a CSV file where the columns contain features of the tracks and spots (Track ID, ellipse aspect ratio, time, spot coordinates in X and Y, mean and total spot intensities, and more). The rows of the features are organized by time point and Track ID. They display the values of each of the features for each time point. In particular, we are interested in the ellipse aspect ratio defined as

$$ellipse\ aspect\ ratio\ =\ ellipse\ long\ axis \div ellipse\ short\ axis \quad \text{(Eq. 4)}$$

The aspect ratio of a perfect circle is 1, whereas for any non-circular object, it will be greater than 1. All analysis of the tracks CSV will be done using python

3.3a Processing the tracks

The tracks CSV was processed to check for the quality of the data and to prepare the data for downstream analysis steps. First, I split the tracks by Track ID to create one data frame per track. The fusion movies should consist of exactly two spots that fuse into one spot. For this reason, I expect two tracks and will not use data where more than two are tracked. Next, I sort each of the data frames by their time column in ascending order. Then, I determine which track is longer as that is the track that is kept after the fusion event.

The next step is to determine the fusion start and end times. I define the fusion start time as the time at which the ellipse aspect ratio is maximal in the longer track. Usually the movies are clipped so that the fusion end time does not need to be calculated. However, if

there is a consecutive fission or other event that causes the droplet to largely deform, I will use the time at which the ellipse aspect ratio is minimal within a user-indicated window before next time the ellipse aspect ratio rises above 1.50.

3.3b Shape analysis: Ellipse aspect ratio vs. time

Once the tracks have been processed, I generate ellipse aspect ratio vs. time graphs using the longer track that tracks the droplet through fusion. Next, I use the *optimize.curve_fit()* function in the *scipy* python package to fit the following exponential model to the data

$$partial\,model \; = \; A^{-kT} + 1 \quad \text{(Eq. 5)}$$
$$full\,model \; = \; A^{-kT} + C \quad \text{(Eq. 6)}$$

in a two-step process, where A, C, and k are constants found through fitting and T is the time. A quantifies the rate of decay of the exponential, C is a constant to scale the fit, and k is such that 1/k measures the time of the fusion event. The partial model introduces a C of 1, which is the expected aspect ratio of a sphere. This is to help the algorithm find a more accurate fit.

Finally, I calculated the R^2 of the exponential fit as defined below.

$$R^2 \; = \; 1 \; - \; (SSr \; \div \; SSt) \quad \text{(Eq. 7)}$$

Where SSr is the residual sum of squares and SSt is the total sum of squares. The A, C, 1/k, and R^2 values are saved to a CSV file and ordered by descending order of R^2.

3.3c Confirming fusion: Velocity and intensity vs. time

Another characteristic that I computed from the track data is the velocity of the particles throughout the fusion event. The velocity is interesting because we expect the velocity of the smaller droplet to increase immediately before fusion due to the phenomenon of osmo ripening. To calculate the velocity, I divide the distance (calculated as per the formula below) by the time between each consecutive time point.

$$distance \; = \; \sqrt{((X1 - X0)^2 \; + \; (Y1 - Y0)^2)} \quad \text{(Eq. 8)}$$

Because this data is extremely noisy, some smoothing was necessary to better visualize the trends in the data. I smoothed the data using the Savitzky-Golay filter using the signal.savgol_filter() method in the *scipy* python package where the window length is the floor of the number of time points in the track and the polynomial degree is 3.

I also plotted the sum of the intensities of each of the Kar9 spots against time. This plot serves as a sanity check because we expect the intensity of the remaining spot to additively increase after the fusion event. This graph was smoothed in the same manner as the velocity vs. time graphs.

3.3d Filtering of the data

Once all of the fusion events have been processed as described in Section 3.3a-c, I set up an exclusion criteria to remove events that may not be truly fusion events, but rather two spots that pass by one another and then drift out of the Z frame. The exclusion criteria also removes data where the exponential fit is extremely poor, and thus unrepresentative of the data. After filtering the data, the remaining data can be used to plot the characteristic fusion time vs. length graph.

Exclusion criteria 1. At the time of fusion, the intensity should be approximately additive. Due to possible measurement errors and possible drifting in the Z-direction, I will not require the intensity to be exactly additive.

Exclusion criteria 2. The R^2 of the exponential fit should be greater or equal to 0.60. This R^2 requirement is relatively low compared to general standards because our data is extremely noisy due to the fast time scale.

3.3e Characteristic fusion time vs. length

The characteristic fusion time, or relaxation time, is the time it takes from the start to the end of fusion. This is defined by 1/k in our analyzed data and I will plot it against the mean diameter of the Kar9 spot during all time points before fusion. Finally, I fit the data to a line using the *polyfit()* function in the *numpy* python package where the input degree is 1, while applying the assumption that the line passes through (0,0).

4 Results

4.1 The pipeline

For all the results below, the data was collected, cropped, and SIM^2 processed as described in Section 3.1. In total, we were able to collect 25 fusion events. Next, using 10 randomly selected slices from the data, I trained a TWS classifier model where class 1 is the Kar9-mNG and class 2 is the background artifacts. Then, I ran each of the 25 fusion events through TrackMate using the TWS detector with the trained model and a probability threshold of 0.8 as inputs. Because the TWS detector is extremely selective, no additional spot or track filters are necessary in general. Next, I ran the output CSV containing the tracks through all the analysis steps detailed in Section 3.3.

4.2 Aspect ratio vs. time shows a sharp spike followed by an exponential decay

The aspect ratio vs. time graphs of the fusion events show that the ellipse aspect ratio, although very noisy, seems to hover between 1.00 and 1.25 until it suddenly increases to around 2.00 before quickly coming down to the initial range (Fig. 3A-C). The exponential fit is a good enough (ie. >= 0.60) around 66% of the time and a poor fit 34% of the time (Fig. 3D).
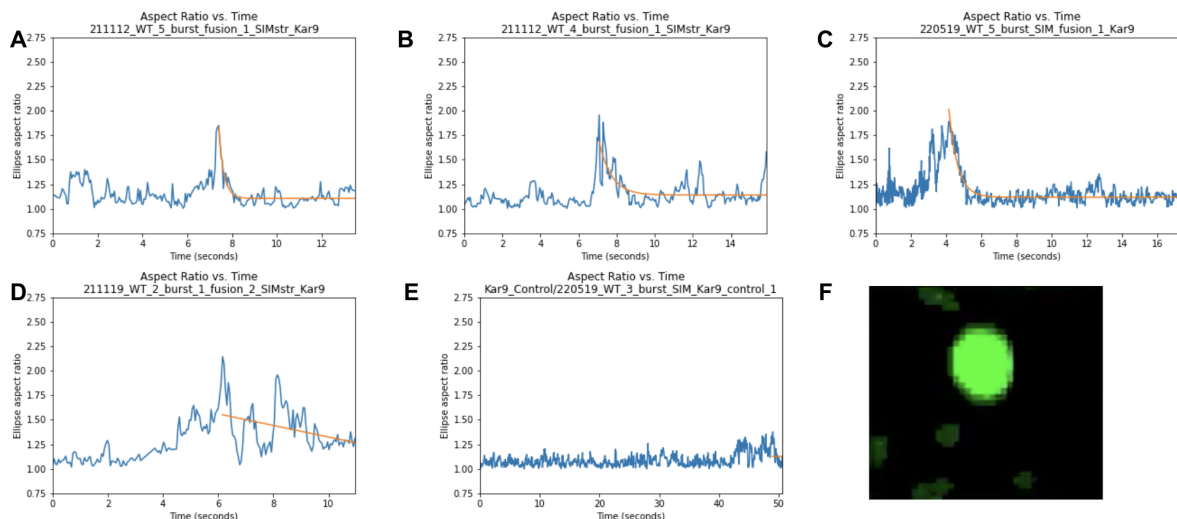
Figure 3. (A-C) Aspect ratio vs. time graphs with good fit ($R^2 >= 0.60$). (D) Randomly selected aspect ratio vs. time graph with poor fit ($R^2 < 0.60$). (E) Aspect ratio vs. time graph of control. (F) SIM^2 processed image of control.

4.3 Negative control non-fusing droplet has no notable spikes in aspect ratio

I also looked at the aspect ratio vs. time graphs of non-fusing Kar9 complexes to use as a negative control. In the negative control, the aspect ratio nearly always hovered between 1.00 and 1.15, and never rose above 1.50 (Fig. 3E-F).

4.4 Velocity and intensity vs. time

The velocity vs. time data was extremely noisy (Fig. 4B) and there was no discernible trend to the velocity even after smoothing (Fig. 4A). Velocity data was only collected for 8 samples.

The intensity vs. time graphs showed in general that the intensity of the spot that is tracked through the fusion event increases at the same time the tracks for the other spot disappears (Fig. 4C). During the time points after the spike, the intensity usually stays relatively high, but there are some short instantaneous dips in some of the intensity values (Fig. 4F).

4.5 Characteristic fusion time vs. length shows slight upward trend [Figure]

After applying the exclusion criteria, there are 18 data points that remain. The range of the diameters of our Kar9 spots is very narrow, ranging only around 0.06 microns. For this reason, it is difficult to visualize a trend for our data. However, there seems to be a slight upward trend where the relaxation time increases with the length. The linear fit R^2 is 0.11.

4.6 Phase control

I also generated an aspect ratio vs. time graph where each represents the data from a single phase of the microscopy acquisition. This is to check that there are no abnormalities in any of the phases that may be disrupting the data. Each line on the graph (Fig. 4D-E)

represents a different phase. There are no discernible differences in the lines representing each of the phases for both the control and the fusion data.
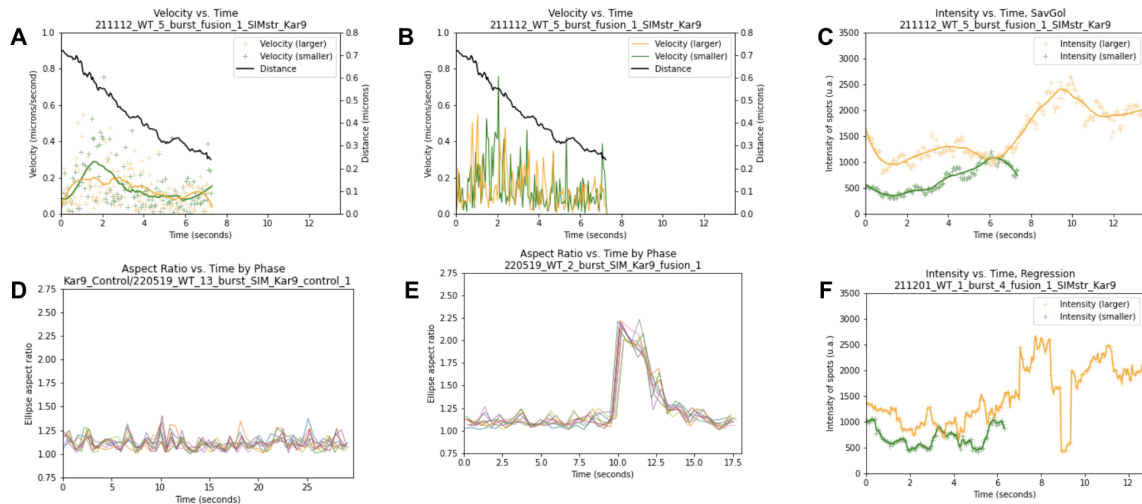

Figure 4. (A) Velocity vs. time graph with Savitzkly-Golay filtering and (B) without. (C) Intensity vs. time graph with Savitzky-Golay filtering. (D) Aspect ratio vs. time graph where each line plots a different phase of the control and (E) the fusion event. (F) Non-smoothed intensity vs. time graphs sometimes show a sudden dip in intensity.

5 Discussion

The high resolution images produced by the Elyra 7.2 SIM^2 microscope system allows us to analyze events in live cells on the nanometer scale. One application of this new device is to study the behaviour of *in vivo* Kar9 by performing shape analysis of observable fusion-like events. The pipeline introduced in this work includes the application of Version 7 ImageJ2 detectors in the TrackMate plugin that require high enough pixel counts to elicit trustworthy results – a requirement that has not previously been met in the context of live cell microscopy of the Kar9 protein with previous technology in the lab. These new detectors offer new features that track information about the spot contours that allow us to study biological events from the perspective of shape analysis.

In our data collection, we reasoned that 2D data would be sufficient for analyzing the fusion-like events of Kar9 complexes. This is because we expect that, as long as the Kar9 complexe is within the focal depth, observing fusion-like is sufficient for understanding the physical properties of the complexe (ie. if one part of the droplet behaves like a droplet, we expect the rest of it to do so as well). Furthermore, we are very selective of the fusion events and will only keep acquisitions where the Kar9 stay centered on the plane through the entire event. 2D images also allow us to quantify the shape using aspect ratio and makes it easier to compare with existing studies.

The TWS model developed in the methods only uses 10 slices of in-sample data labeled by people directly involved in this study. The fact that all the data is labeled by people working on this study is a possible source of bias because of our expected results. Therefore,

we propose the addition of training data labeled by people who have no knowledge of the study. From our segmentation results, it looks like 10 slices is sufficient to train the model, but we should include more slices with the addition of externally-labeled data.

The aspect ratio vs. time graphs seem to corroborate our hypothesis that the fusion event follows an exponential curve. Although about a third of the data is a poor fit, it is important to note that for many of the poore fit examples, the microscopy movie ended very shortly after the fusion event, which might have prevented the exponential tail from forming. One way to alleviate this problem is to take longer movies, but the tradeoff here will be a longer SIM^2 processing time. Another reason for poor fit is because our data is very noisy due to the intracellular environment, which contains a high concentration of different molecules and where Brownian forces tend to dominate. I tried to account for this by lowering the R^2 threshold below which the data points will be discarded. A possible follow up to this issue would be to study different ways of measuring goodness-of-fit that is more suitable for noisy data. The exponential decay of the aspect ratio after a fusion event indicates the likelihood that the Kar9 complexe is exhibiting droplet-like properties, where the surface tension of the energetically unfavourable dumbbell shape during fusion quickly collapses into the energetically more favourable sphere.

The negative control for the aspect ratio vs. time graphs confirms that the aspect ratio values are reasonable in the case of the non-fusing particles. This suggests that the values obtained for the fusion events should be reasonable as well. Another possible negative control is to use TetraSpeck beads that collide but do not fuse to confirm that collision events look different from fusion events. In an ideal scenario, there should also be a positive control. However, that is difficult to engineer biologically.

The velocity vs. time graphs did not show any noticeable trends, largely because the data was extremely noisy. I believe this is partly because of the environment where the particles are in a very crowded and random environment. Perhaps there are better methods to capture the velocity, such as taking the average position over a sliding window.

The intensities over time seem to corroborate our hypothesis that there will be an additive increase in the intensity after the fusion event. I also observed some short dips in the intensity after the fusion event in a few of the raw, unsmoothed graphs. This could possibly be a result of the Kar9 complexe drifting in the Z-direction. However, this suggests that it might be a good idea to look at the unsmoothed intensity data to extract information about the Z-axis, which is not captured in the microscopy data.

The characteristic fusion time of the fusion-like events seem to be somewhat positively correlated with the diameter of the Kar9 complexe. However, because our experiments are *in vivo* and look exclusively at wild type budding yeast, we have a very narrow distribution of Kar9 lengths in the graph. Perhaps in the future, we can look at mutants, such as a multivalency mutant which has fewer bonding sites and will therefore form smaller condensates in theory. Furthermore, it is important to address the low R^2 value ($R^2 = 0.11$) of the linear fit. Although this value is very low, our data and fit are visually very similar to a previous study that confirmed *in vitro* Kar9 condensates (Meier et. al., 2021) that was accepted by Nature [Figure]. Furthermore, perhaps the R^2 value will improve with a wider length distribution, which could be obtained from mutants.

The next steps to this study is to increase the size of the data set, examine different strains, and implement additional negative and positive controls. The preliminary results suggest that we are indeed observing fusion events of liquid-like condensates of Kar9 protein. However, it would be ideal to biochemically confirm, perhaps through proximity sensors fluorescent microscopy, that the two droplets are indeed mixing.
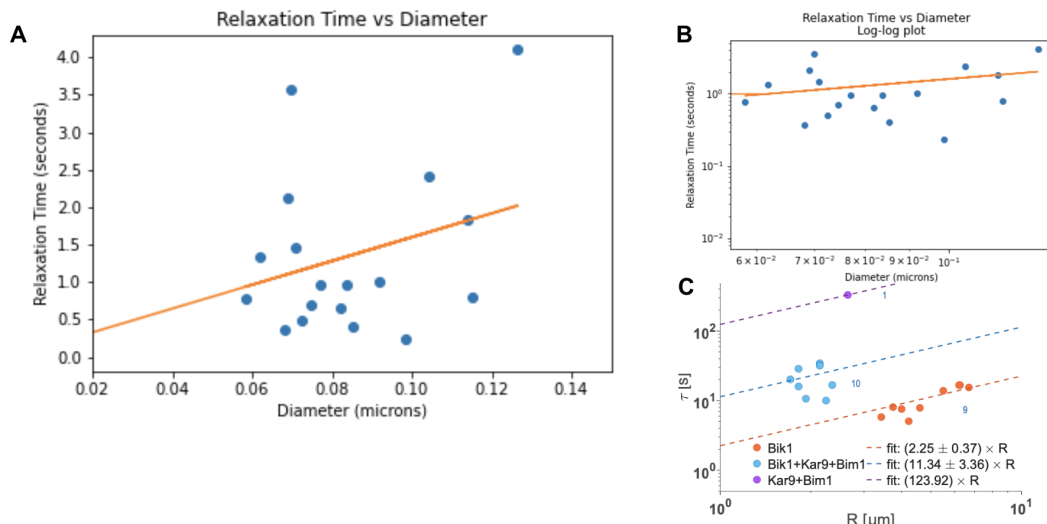

Figure 5. (A) Characteristic fusion time vs. diameter graph with linear fit (R^2 = 0.11). (B) Same graph as (A) on a log-log scale. (C) Graph from Meier et. al., 2021 for comparison showing in vitro data of wild type (blue) and mutant Kar9 droplets.

6   Conclusions

This work combines important concepts in biology, physics, and computer science to study the physical properties of Kar9 fusion-like events during spindle positioning. We employed the cutting-edge Elyra 7.2 SIM^2 system and developed a machine learning-based shape analysis pipeline to preliminarily confirm droplet-like properties in the Kar9 protein. This pipeline will be used in future studies for studying wild type and mutant budding yeast Kar9 fusion events. The machine learning-based segmentation tool can be repurposed to other Elyra 7.2 SIM^2 microscopy data and will be a powerful asset to decthe artifacts generated by SIM^2 processing.

References

Arganda-Carreras, I., Kaynig, V., Rueden, C., Eliceiri, K. W., Schindelin, J., Cardona, A., & Sebastian Seung, H. (2017). Trainable weka segmentation: A machine learning tool for microscopy pixel classification. *Bioinformatics, 33*(15), 2424-2426. doi:10.1093/bioinformatics/btx180

Brangwynne, C. P., Mitchison, T. J., & Hyman, A. A. (2011). Active liquid-like behavior of nucleoli determines their size and shape in *xenopus laevis* oocytes. *Proceedings of the National Academy of Sciences, 108*(11), 4334-4339. doi:10.1073/pnas.1017150108

Chen, X., Widmer, L. A., Stangier, M. M., Steinmetz, M. O., Stelling, J., & Barral, Y. (2019). Remote control of microtubule plus-end dynamics and function from the minus-end. *ELife, 8*. doi:10.7554/elife.48627

EGGERS, J., LISTER, J. R., & STONE, H. A. (1999). Coalescence of Liquid Drops. *Journal of Fluid Mechanics, 401*, 293-310. doi:10.1017/s002211209900662x

He, K., Gkioxari, G., Dollar, P., & Girshick, R. (2017). Mask R-CNN. *2017 IEEE International Conference on Computer Vision (ICCV)*. doi:10.1109/iccv.2017.322

Hotz, M., Leisner, C., Chen, D., Manatschal, C., Wegleiter, T., Ouellet, J., . . . Barral, Y. (2012). Spindle pole bodies exploit the mitotic exit network in metaphase to drive their age-dependent segregation. *Cell, 148*(5), 958-972. doi:10.1016/j.cell.2012.01.041

Jaqaman, K., Loerke, D., Mettlen, M., Kuwata, H., Grinstein, S., Schmid, S. L., & Danuser, G. (2008). Robust single-particle tracking in live-cell time-lapse sequences. *Nature Methods, 5*(8), 695-702. doi:10.1038/nmeth.1237

Kumar, A., Meier, S. M., Farcas, A., Manatschal, C., Barral, Y., & Steinmetz, M. O. (2021). Structure and regulation of the microtubule plus-end tracking protein Kar9. *Structure, 29*(11). doi:10.1016/j.str.2021.06.012

Liu, W., Anguelov, D., Erhan, D., Szegedy, C., Reed, S., Fu, C., & Berg, A. C. (2016). SSD: Single shot multibox detector. *Computer Vision – ECCV 2016,* 21-37. doi:10.1007/978-3-319-46448-0_2

Lowe, D. G. (2004). Distinctive image features from scale-invariant keypoints. *International Journal of Computer Vision, 60*(2), 91-110. doi:10.1023/b:visi.0000029664.99615.94

Manatschal, C., Farcas, A., Degen, M. S., Bayer, M., Kumar, A., Landgraf, C., . . . Steinmetz, M. O. (2016). Molecular basis of Kar9-BIM1 complex function during mating and spindle positioning. *Molecular Biology of the Cell, 27*(23), 3729-3745. doi:10.1091/mbc.e16-07-0552

Meier, S. M., Farcas, A., Kumar, A., Ijavi, M., Bill, R. T., Stelling, J., . . . Barral, Y. (2021). High interaction valency ensures cohesion and persistence of a microtubule +tip body at the plus-end of a single specialized microtubule in yeast. doi:10.1101/2021.09.13.460064

Meziane, M., Genthial, R., & Vogel, J. (2020). Spindle alignment is uncoupled with KAR9 symmetry breaking. doi:10.1101/2020.09.01.278523

Miller, R. K., & Rose, M. D. (1998). Kar9p is a novel cortical protein required for cytoplasmic microtubule orientation in yeast. *Journal of Cell Biology, 140*(2), 377-390. doi:10.1083/jcb.140.2.377

Moore, J. K., D'Silva, S., & Miller, R. K. (2006). The clip-170 homologue bik1p promotes the phosphorylation and asymmetric localization of Kar9p. *Molecular Biology of the Cell, 17*(1), 178-191. doi:10.1091/mbc.e05-06-0565

Pereira, G. (2001). Modes of spindle pole body inheritance and segregation of the BFA1P-bub2p checkpoint protein complex. *The EMBO Journal, 20*(22), 6359-6370. doi:10.1093/emboj/20.22.6359

SCHAEFER, L. H., SCHUSTER, D., & SCHAFFER, J. (2004). Structured illumination microscopy: Artefact analysis and reduction utilizing a parameter optimization approach. *Journal of Microscopy, 216*(2), 165-174. doi:10.1111/j.0022-2720.2004.01411.x

Schmidt, U., Weigert, M., Broaddus, C., & Myers, G. (2018). Cell detection with star-convex polygons. *Medical Image Computing and Computer Assisted Intervention – MICCAI 2018,* 265-273. doi:10.1007/978-3-030-00934-2_30

Stone, H. A. (1994). Dynamics of drop deformation and breakup in viscous fluids. *Annual Review of Fluid Mechanics, 26*(1), 65-102. doi:10.1146/annurev.fl.26.010194.000433

Tinevez, J., Perry, N., Schindelin, J., Hoopes, G. M., Reynolds, G. D., Laplantine, E., . . . Eliceiri, K. W. (2017). TrackMate: An open and extensible platform for single-particle tracking. *Methods, 115*, 80-90. doi:10.1016/j.ymeth.2016.09.016

Trackmate V7 detectors. (n.d.). Retrieved May 30, 2022, from https://imagej.net/plugins/trackmate/trackmate-v7-detectors

Zeiss Elyra 7 with lattice sim² super-resolution microscope. (n.d.). Retrieved August 10, 2022, from https://www.zeiss.com/microscopy/en/products/light-microscopes/widefield-microscopes/elyra-7.html

Zimniak, T., Stengl, K., Mechtler, K., & Westermann, S. (2009). Phosphoregulation of the budding yeast EB1 homologue Bim1p by Aurora/IPL1P. *Journal of Cell Biology, 186*(3), 379-391. doi:10.1083/jcb.200901036